

Feedback Assisted Spin Dynamics in an Inhomogeneous Bias Magnetic Field

Tishuo Wang,^{1,2} Zhihuang Luo,^{1,2,*} Shizhong Zhang,³ and Zhenhua Yu^{1,2,†}

¹Guangdong Provincial Key Laboratory of Quantum Metrology and Sensing,
and School of Physics and Astronomy, Sun Yat-Sen University (Zhuhai Campus), Zhuhai 519082, China

²State Key Laboratory of Optoelectronic Materials and Technologies,
Sun Yat-Sen University (Guangzhou Campus), Guangzhou 510275, China

³Department of Physics and HKU-UCAS Joint Institute for Theoretical and Computational Physics at Hong Kong,
The University of Hong Kong, Hong Kong, China

(Dated: February 13, 2023)

We study dynamics of spins in the presence of a feedback magnetic field. The inhomogeneity of the bias magnetic field results in that of the Larmor frequencies of the spins. We find that the system exhibits rich nonlinear dynamics: beyond limit cycles which have been the focus of previous studies, quasi-periodic orbits and chaos emerge in a wide parameter space. The stable regions of each phases are determined analytically or numerically. We establish the relation between the synchronization frequency of limit cycles and the field inhomogeneity. Our results have important implications to precision measurement.

PACS numbers:

Introduction.—Spin dynamics offers a unique window to investigate the magnetic properties of physical systems [1]. Recent developments have further extended its applications to quantum computation [2] and quantum metrology [3]. Introduction of feedback mechanisms has led to the advance in spin maser technologies [4–6]. Subsequently, extensive studies on the properties of spin masers in noble gases, due to their long spin coherent times, have been performed [7–10]. The continuously improved precision of spin masers [11–15] makes them promising in the search of permanent electric dipole moments [16, 17], and tests of fundamental physics beyond the standard model [18–20].

The spin masers are operating in a bias magnetic field. How the inhomogeneity of the field affects the performance of the spin systems is a primary concern regarding precision measurement. When the diffusion time τ_D is short, the effect of the inhomogeneity can be taken into account by quantitatively modifying the spin relaxation times and result in the motional narrowing of resonance linewidth [21–23]. When the diffusion is slow, application of a magnetic field gradient is found to suppress the masing threshold, and leads to a broadening of the masing frequency at the threshold [24]. However, the fate of spin dynamics in such systems in a broader parameter space awaits further investigation.

In this work, we study the dynamics of a collection of spins that are subjected to a feedback magnetic field in addition to a static inhomogeneous bias magnetic field. We found that the system exhibits rich nonlinear dynamical phases that include limit cycles, quasi-periodic orbits and chaos. In the phase of limit cycles, the spins synchronize their oscillations at a single frequency. The

dependence of the synchronized frequency on the inhomogeneity is derived. In the phase of quasi-periodic orbits, the Fourier transform of the transverse spin component peaks at frequencies with equal spacing. The chaotic motion exhibits close resemblance to the butterfly pattern of the well-known Lorenz equations. By both analytic and numerical methods, we determine the stable regions of each phases. Finally we discuss the experimental testing of our conclusions and the implication of our results to precision measurement.

Formalism.—We consider a collection of N spins in a static bias magnetic field \mathbf{B} along the \hat{z} -direction, whose dynamics is governed by the Bloch equations ($\hbar = 1$)

$$\frac{dP_{j,x}}{dt} = \omega_j P_{j,y} - \gamma B_y P_{j,z} - \frac{P_{j,x}}{T_2}, \quad (1)$$

$$\frac{dP_{j,y}}{dt} = -\omega_j P_{j,x} + \gamma B_x P_{j,z} - \frac{P_{j,y}}{T_2}, \quad (2)$$

$$\frac{dP_{j,z}}{dt} = \gamma B_y P_{j,x} - \gamma B_x P_{j,y} - \frac{P_{j,z}}{T_1} + G(P_0 - P_{j,z}). \quad (3)$$

Here $\mathbf{P}_j = (P_{j,x}, P_{j,y}, P_{j,z})$ is the expectation value of the j -th spin operator. The Larmor frequency for each spin ω_j can be different due to the inhomogeneity of \mathbf{B} . The longitudinal and transverse relaxation times are T_1 and T_2 respectively. The spins are also subjected to pumping with rate G with P_0 a constant, and γ is the gyromagnetic ratio of the spins. Simultaneously, all spins are subjected to an artificial feedback magnetic field $B_x(t) = \alpha \bar{P}_y(t)/\gamma$ and $B_y(t) = -\alpha \bar{P}_x(t)/\gamma$ that are proportional to the instantaneous average spin polarization $\bar{\mathbf{P}}(t) \equiv (1/N) \sum_{j=1}^N \mathbf{P}_j(t)$ with $\alpha (> 0)$ the amplification factor. In the case when the bias magnetic field is homogeneous, i.e., ω_j are identical, it has been shown that the no signal fixed point $\mathbf{P}_j = \mathbf{P}_{NS} \equiv (0, 0, P_0/(1 + 1/GT_1))$, corresponding to zero transverse spin polarization, becomes unstable once α exceeds the critical value $\alpha_c \equiv (1 + 1/GT_1)/T_2 P_0$. For $\alpha > \alpha_c$, a new stable limit cycle solution emerges for which a non-zero transverse spin

*luozhih5@mail.sysu.edu.cn

†huazhenyu2000@gmail.com

polarization processes at the identical Larmor frequency, corresponding to the onset of maser [8].

Binary Larmor frequencies.—To investigate the effects of an inhomogeneous bias magnetic field, we start with a simpler model, considering the situation of a binary Larmor frequencies in which half of the spins are subject to $\omega_1 = \omega_c + \epsilon/2$ and the other half $\omega_2 = \omega_c - \epsilon/2$. Without loss of generality, we assume $\epsilon > 0$. In this case, we only need to consider two representative spins \mathbf{P}_1 and \mathbf{P}_2 , equivalent to taking $N = 2$ in Eqs. (1) to (3). The differential equations of this binary case are of six dimensions and trajectories obtained by numerically solving these equations would be rather difficult to analyze and visualize. In experiment, however, the spins are usually prepared in the same initial state. By assuming that initially $\mathbf{P}_1(t = 0) = \mathbf{P}_2(t = 0)$, we can prove that subsequent evolution satisfies $P_{1,z} = P_{2,z}$ and $P_{1,x}^2 + P_{1,y}^2 = P_{2,x}^2 + P_{2,y}^2$ at any time t [25]. These two equalities reduce the dimension of the nonlinear dynamic system. Let us define the transverse component $P_{j,T} \equiv P_{j,x} + iP_{j,y}$ and the difference $\Delta P_T \equiv P_{1,T} - P_{2,T}$. The second equality then ensures that \bar{P}_T must always be perpendicular to ΔP_T , thus prompting us to parameterize $\bar{P}_T = Ae^{i\theta}/2$ and $\Delta P_T = Be^{i(\theta+\pi/2)}$ with amplitudes A and B and phase angle θ being real. The resulting dynamic equations become

$$\frac{dA}{dt} = \alpha \bar{P}_z A + \frac{\epsilon B}{2} - \frac{A}{T_2}, \quad (4)$$

$$\frac{dB}{dt} = -\frac{\epsilon A}{2} - \frac{B}{T_2}, \quad (5)$$

$$\frac{d\bar{P}_z}{dt} = -\frac{\alpha A^2}{4} - \frac{\bar{P}_z}{T_1} + G(P_0 - \bar{P}_z), \quad (6)$$

$$\frac{d\theta}{dt} = -\omega_c. \quad (7)$$

Since the phase angle can be readily solved as $\theta(t) = -\omega_c t + \phi$, the remaining dynamic system is simplified to three-dimension for unknowns $\{A, B, \bar{P}_z\}$. Thus, in the following, whenever stable dynamics of the system (regardless initial conditions) maintains the two equalities, we apply the dimension reduction to simplify the analysis and visualization of the corresponding trajectories.

Figure 1 gives the stability diagram for the case of binary Larmor frequencies. The system is found to exhibit rich stable dynamical phases including limit cycles, quasi-periodic orbits and chaos in different regimes. In the presence of inhomogeneity, now the no signal fixed point becomes unstable when α/α_c exceeds $f(\epsilon T_2)$ with $f(x) \equiv 1 + (x/2)^2$ for $\epsilon T_2 < 2$ and $f(x) \equiv 2$ for $\epsilon T_2 > 2$. For $\alpha/\alpha_c > f(\epsilon T_2)$ and smaller value of ϵT_2 , there exists a limit cycle solution given by $P_{1,T} = \alpha \bar{P}_T P_{1,z}/(1/T_2 + i\epsilon/2)$, $P_{2,T} = \alpha \bar{P}_T P_{2,z}/(1/T_2 - i\epsilon/2)$, $P_{1,z} = P_{2,z} = f(\epsilon T_2)/\alpha T_2$ with $\bar{P}_T = e^{-i(\omega_c t - \phi)} \{GP_0[\alpha - \alpha_c f(\epsilon T_2)]\}^{1/2}/\alpha$ [see Figs. 2(a) and 2(c)]; the two spins synchronize and remain static in the frame rotating with the center frequency ω_c .

Since the dimension reduction is applicable in the

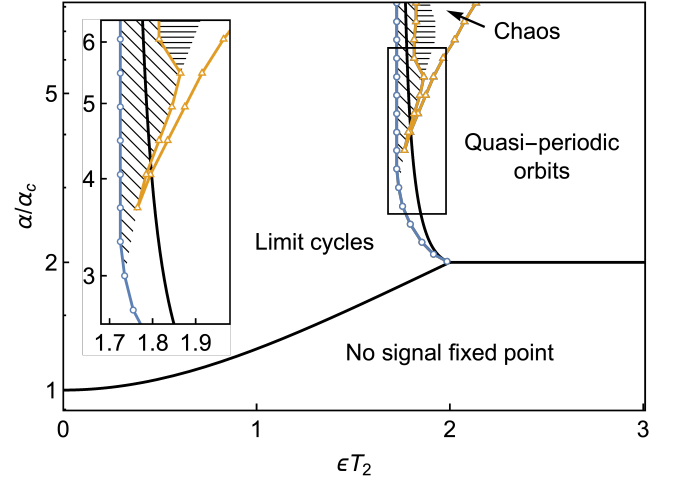


FIG. 1: Stability diagram for the case of binary Larmor frequencies. Linear stability analysis determines the phase boundaries of both the no signal and limit cycle regions, which are shown as (black) solid lines. The stable region of the no signal fixed point is given by $\alpha/\alpha_c < 1 + (\epsilon T_2/2)^2$ for $\epsilon T_2 < 2$ and $\alpha/\alpha_c < 2$ for $\epsilon T_2 > 2$. The limit cycles are stable in the region left to the (black) solid line whose analytical expression is $\alpha/\alpha_c = 3y/2 + (1-d)/2(y-d)$ with $y \equiv (\epsilon T_2/2)^2$ and $d \equiv T_2(G+1/T_1)$ as $\min(1, d) < y < \max(1, d)$; for the parameters taken for calculation, $d = 0.77$. The symbols of triangle and circle mark the boundaries of the stable regions of the chaos and quasi-periodic orbits determined numerically. The lines linking the symbols are guide for the eye. There exist overlaps of the stable regions. The two equalities, $P_{1,z} = P_{2,z}$ and $P_{1,x}^2 + P_{1,y}^2 = P_{2,x}^2 + P_{2,y}^2$, are found to hold numerically except for the quasi-periodic orbits in the diagonally slashed area and for the chaos in the horizontally slashed area. The inset shows a zoom-in of the boxed part.

phase with the limit cycle solution, their stable region can be readily worked out via a linear stability analysis [25]. In terms of $\{A, B, \bar{P}_z\}$, the limit cycle solution is represented by a pair of twin fixed points $A_{LC,\pm} = \pm 2\{GP_0[\alpha - \alpha_c f(\epsilon T_2)]\}^{1/2}/\alpha$, $B_{LC,\pm} = -\epsilon T_2 A_{LC,\pm}/2$ and $\bar{P}_{z,LC} = f(\epsilon T_2)/\alpha T_2$ [see Fig. 2(b)]; the two fixed points correspond to two inequivalent periodic orbits of the limit cycles whose phase angles ϕ differ by π . Linear stability analysis using Eqs. (4) to (6) shows that the limit cycles are stable, as shown in Fig. 1, left to the line $\alpha/\alpha_c = 3y/2 + (1-d)/2(y-d)$ with $y \equiv (\epsilon T_2/2)^2$ and $d \equiv T_2(G+1/T_1)$ as $\min(1, d) < y < \max(1, d)$. Therefore, no stable limit cycles exist beyond the line $y = \max(1, d)$ no matter how strong α is. Crossing the line from the left side to the right accompanies a Hopf bifurcation.

More generally, beyond the linear stability analysis, we can determine the stable dynamical phases numerically. In the following, we use the following parameters $P_0 = 0.8$, $1/T_1 = 0.111$ Hz, $1/T_2 = 0.148$ Hz, $\omega_c/2\pi = 8.85$ Hz and $G = 0.00248$ Hz [9] for numerical calculation. In this way, we found regions with stable quasi-periodic orbits and chaotic behavior. Note that

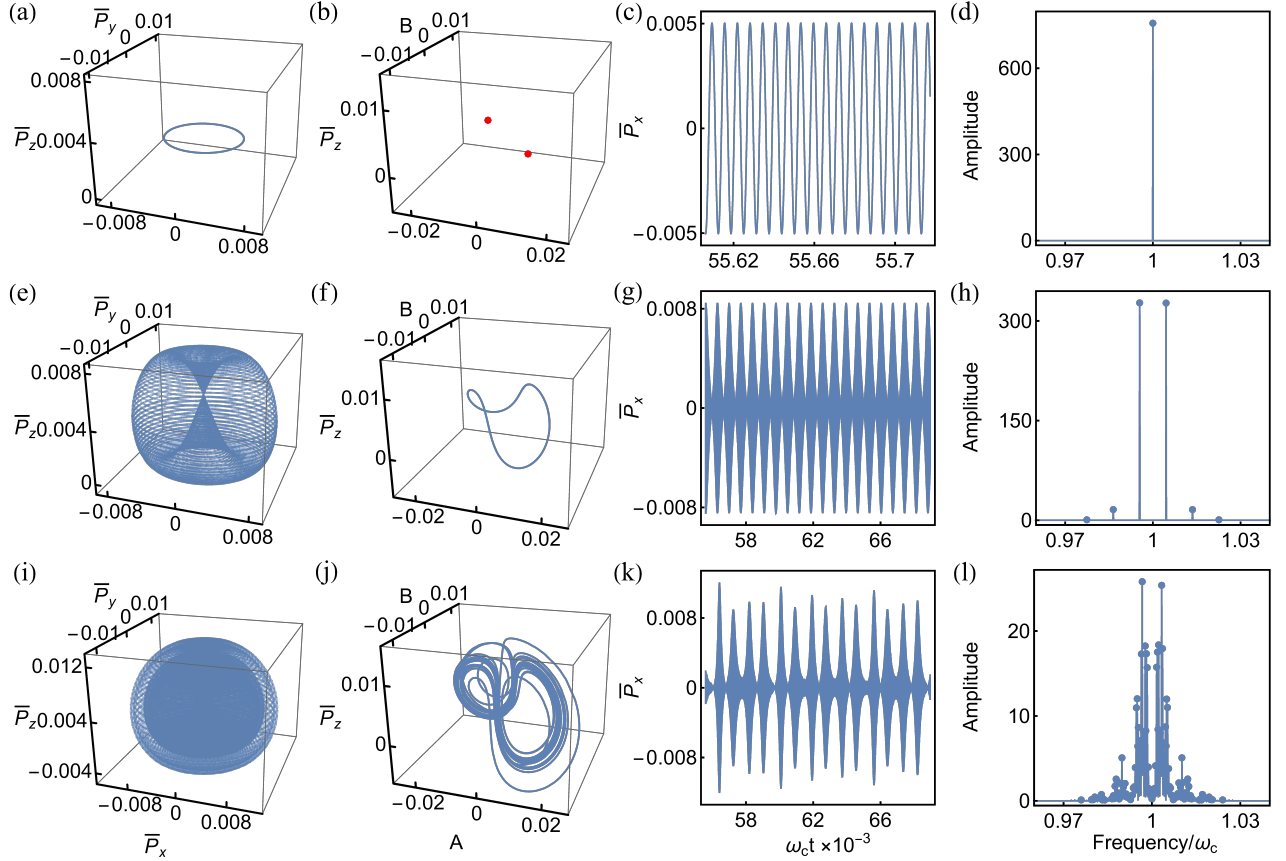


FIG. 2: Stable dynamic behavior in the case of binary Larmor frequencies. (a)~(d) are for the limit cycles at $\alpha/\alpha_c = 8$, $\epsilon T_2 = 1.5$, (e)~(h) for the quasi-periodic orbits at $\alpha/\alpha_c = 8$, $\epsilon T_2 = 3$, and (i)~(l) for the chaos at $\alpha/\alpha_c = 8$, $\epsilon T_2 = 2.2$. The first column of the graphs plot the trajectories of the average spin polarization $\bar{\mathbf{P}}(t)$, and the second are the corresponding trajectories in the phase space of $\{A, B, \bar{P}_z\}$. When represented in terms of $\{A, B, \bar{P}_z\}$, the limit cycles condense into two fixed points ($A_{LC,\pm}, B_{LC,\pm}, \bar{P}_{z,LC}$), the quasi-periodic orbits unify into a limit cycle solution, and the chaotic trajectories are reminiscent of the renowned Lorenz equations. The third column show the time series of $\bar{P}_x(t)$ and the forth are the Fourier transform amplitudes of $\bar{P}_x(t)$ in arbitrary units.

these two regions of long time stable dynamics extend to the region of limit cycles; in the overlapped regions, the long time stable dynamics depends on initial conditions. In Fig. 1, the symbols of triangle and circle mark the numerical boundaries of the stable regions of the chaos and quasi-periodic orbits; the lines linking the symbols are guide for the eye. Interestingly, our numerical calculation indicates that the two equalities $P_{1,z} = P_{2,z}$ and $P_{1,x}^2 + P_{1,y}^2 = P_{2,x}^2 + P_{2,y}^2$ also hold for the quasi-periodic orbits and chaotic phases except for the slashed areas zoomed in in the inset.

Figure 2 shows the stable dynamic behavior of the limit cycles, quasi-periodic orbits and chaos in the parameter range where the two equalities are maintained and the dimension reduction is applicable. For the quasi-periodic orbits, the trajectories of $\bar{\mathbf{P}}(t)$ look rather dense as shown in Fig. 2(e). However, once represented in terms of $\{A, B, \bar{P}_z\}$, the quasi-periodic orbits unify into a limit cycle solution as shown in Fig. 2(f). Note that this limit

cycle solution generally has a three dimensional configuration, and its period τ , while independent of ω_c , changes with α and ϵ [25]. Since if $(A(t), B(t), \bar{P}_z(t))$ is a solution to Eqs. (4) to (6), so is $(-A(t), -B(t), \bar{P}_z(t))$, it is easy to prove that the limit cycle solution corresponding to the quasi-periodic orbits satisfies $A(t) = -A(t + \tau/2)$, $B(t) = -B(t + \tau/2)$ and $\bar{P}_z(t) = \bar{P}_z(t + \tau/2)$. Therefore the Fourier transform amplitude of $\bar{P}_x(t)$ or $\bar{P}_y(t)$ peaks at regular frequencies $\omega_c + 2\pi(2n+1)/\tau$ with integer n as shown in Fig. 2(h). In contrast, the chaotic trajectories in Fig. 2(i), when plotted in terms of $\{A, B, \bar{P}_z\}$ as in Fig. 2(j), are reminiscent of the butterfly pattern of the renowned Lorenz equations. Figure 2(l) shows that the Fourier transform of the chaos peaks irregularly. Within the slashed areas of Fig. 1, either the quasi-periodic orbits or chaos break the two equalities $P_{1,z} = P_{2,z}$ and $P_{1,x}^2 + P_{1,y}^2 = P_{2,x}^2 + P_{2,y}^2$; though the dimension reduction is no longer applicable, their phase portraits are nevertheless similar to Fig. 2(e,g,h) and (i,k,l) [25].

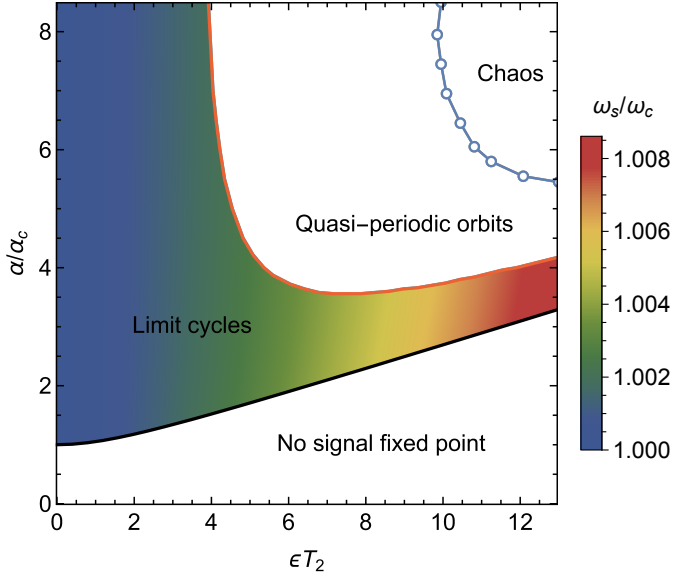


FIG. 3: Stability diagram for the triangle distribution $\rho_T(\omega)$ in the continuum limit. The boundaries separating the stable regions of the no signal fixed point, the limit cycles and the quasi-periodic orbits are plotted by using Eqs. (10) and (11). The solid circles mark the boundary of the stable region of the chaos determined numerically. The line linking the circles is guide for the eye. The shading highlights the variation of the synchronization frequency ω_s in the stable region of the limit cycles.

Continuum limit.— The rich dynamics discovered in the case of binary Larmor frequencies is expected to persist in general situations when the Larmor frequencies ω_j experienced by the N spins are different. In the continuum limit where ω_j distributes according to a nor-

malized density function $\rho(\omega)$, we can continue to label the spins with Larmor frequency ω as $\mathbf{P}(\omega)$. The quantities $\mathbf{P}(\omega)$ continue to satisfy the Bloch equations (1) to (3), in which the Larmor frequency ω_j shall be replaced by ω , and the average spin polarization is given by $\bar{\mathbf{P}} = \int_{-\infty}^{\infty} d\omega \rho(\omega) \mathbf{P}(\omega)$.

In the continuum limit, the limit cycle solution can be derived in the following way. As learned from the binary case, we assume that individual spins synchronize and the synchronization frequency ω_s is to be self-consistently determined as below. After defining $P_T(\omega) \equiv P_x(\omega) + iP_y(\omega)$ and transforming to the rotating frame $\tilde{P}_T(\omega) \equiv e^{i\omega_s t} P_T(\omega)$ and $\tilde{\tilde{P}}_T \equiv e^{i\omega_s t} \tilde{P}_T$, we make use of the self-consistent condition $\tilde{\tilde{P}}_T = \int_{-\infty}^{\infty} d\omega \rho(\omega) \tilde{\tilde{P}}_T(\omega)$ and the Bloch equations to derive

$$0 = \int_{-\infty}^{\infty} \frac{\rho(\omega)(\omega - \omega_s)d\omega}{(G + 1/T_1)[1 + (\omega - \omega_s)^2 T_2^2] + \alpha^2 T_2 |\tilde{\tilde{P}}_T|^2} \quad (8)$$

$$\frac{1}{\alpha G P_0 T_2} = \int_{-\infty}^{\infty} \frac{\rho(\omega)d\omega}{(G + 1/T_1)[1 + (\omega - \omega_s)^2 T_2^2] + \alpha^2 T_2 |\tilde{\tilde{P}}_T|^2}, \quad (9)$$

These two equations jointly determine the signal frequency ω_s and the amplitude $\tilde{\tilde{P}}_T$ up to an arbitrary phase. Consequently for individual spins labeled by ω , $\tilde{P}_T(\omega) = \alpha P_z(\omega) \tilde{\tilde{P}}_T / [1/T_2 + i(\omega - \omega_s)]$ and $P_z(\omega) = G P_0 / \{G + 1/T_1 + \alpha^2 T_2 |\tilde{\tilde{P}}_T|^2 / [1 + (\omega - \omega_s)^2 T_2^2]\}$. In case $\rho(\omega)$ is a symmetric function with respect to a frequency ω_0 , Eq. (8) yields that the synchronized frequency ω_s must be ω_0 .

The stability of the above limit cycle solution can be analyzed by introducing small deviations with growth rate β [25]. We find that β satisfies

$$\left\{ 1 - \alpha \int_{-\infty}^{\infty} d\omega \rho(\omega) [\mathcal{M}_{22}^{-1} P_z(\omega) - \mathcal{M}_{21}^{-1} \tilde{P}_T^*(\omega)/2] \right\} \left\{ 1 - \alpha \int_{-\infty}^{\infty} d\omega \rho(\omega) [\mathcal{M}_{33}^{-1} P_z(\omega) - \mathcal{M}_{31}^{-1} \tilde{P}_T(\omega)/2] \right\} \\ = \alpha^2 \left\{ \int_{-\infty}^{\infty} d\omega \rho(\omega) [\mathcal{M}_{23}^{-1} P_z(\omega) - \mathcal{M}_{21}^{-1} \tilde{P}_T(\omega)/2] \right\} \left\{ \int_{-\infty}^{\infty} d\omega \rho(\omega) [\mathcal{M}_{32}^{-1} P_z(\omega) - \mathcal{M}_{31}^{-1} \tilde{P}_T^*(\omega)/2] \right\}, \quad (10)$$

with \mathcal{M}^{-1} being the inverse matrix of

$$\mathcal{M} = \begin{bmatrix} \beta + G + \frac{1}{T_1} & \alpha \tilde{\tilde{P}}_T^*/2 & \alpha \tilde{\tilde{P}}_T/2 \\ -\alpha \tilde{\tilde{P}}_T & \beta + \frac{1}{T_2} + i(\omega - \omega_s) & 0 \\ -\alpha \tilde{\tilde{P}}_T^* & 0 & \beta + \frac{1}{T_2} - i(\omega - \omega_s) \end{bmatrix}. \quad (11)$$

The limit cycles become unstable whenever the solution of complex β to Eq. (10) can have a *positive* real part. When setting $\tilde{\tilde{P}}_T$ to zero, Eqs. (10) and (11) determine

the stable region of the no signal fixed point.

Application of the binary distribution $\rho_B(\omega) = [\delta(\omega - \omega_1) + \delta(\omega - \omega_2)]/2$ to Eqs. (8), (9) and (10) recovers our previous results for the case of binary Larmor frequencies. Figure 3 shows the stability diagram for the triangle distribution $\rho_T(\omega) = [\theta(\omega - \omega_c + \epsilon/2) - \theta(\omega - \omega_c - \epsilon/2)] \times 2(\omega_c + \epsilon/2 - \omega)/\epsilon^2$, which approximates the situation that the bias magnetic field has a gradient along the direction of the gravitational force and the density of the spins has the Boltzmann distribution due to the force. Similar to the case of binary Larmor frequencies, the limit cycles, quasi-periodic orbits and chaos are found to be stable in

different regions shown in Fig. 3. The boundaries separating the stable regions of the no signal fixed point, the limit cycles and the quasi-periodic orbits are plotted by using Eqs. (10) and (11). The stable region of the chaos is determined numerically. The shading highlights that the synchronization frequency ω_s varies across the stable region of the limit cycles. The stable dynamic behavior in different regions is similar to the case of binary Larmor frequencies as well [25]. Within the range shown in Fig. 3, however, we did not find numerically any overlapping stable regions as for the binary case.

Discussion.— Our conclusions for the case of binary Larmor frequencies can be checked in experiment of a dual spin maser setup [26]: two identical cells consisting of noble gases, such as ^{129}Xe , while placed under distinct bias magnetic fields, are simultaneously subject to the same feedback magnetic field determined by the net spin polarization of all the gas atoms. Co-located nuclear spin masers consisting of two species of atoms, for example, ^{129}Xe and ^{131}Xe , are employed to mitigate the frequency instability due to the magnetic field and cell temperature drifts [14]. Our study indicates that these co-located nu-

clear spin masers shall operate in the quasi-periodic orbit regime. This observation improves our understanding of the true character of the two experimentally extracted frequencies which are presumed to be the Larmor frequencies for ^{129}Xe and ^{131}Xe nuclear spins. Equations (8) and (9) reveal the dependence of the synchronization frequency ω_s on the inhomogeneity of the bias magnetic field via $\rho(\omega)$. This result may also be used to quantify field inhomogeneity in precision measurement.

Acknowledgements.—We thank Xiaodong Li and Long Wang for discussions on numerics. TW and ZY are supported by the National Natural Science Foundation of China Grant No.12074440, and Guangdong Project (Grant No. 2017GC010613). ZL is supported by the National Natural Science Foundation of China Grant No. 11805008, and Guangdong Provincial Key Laboratory (Grant No. 2019B121203005). SZ is supported by grants from the Research Grants Council of the Hong Kong Special Administrative Region, China (HKU 17304719, HKU C7012-21GF and a RGC fellowship award HKU RFS2223-7S03).

-
- [1] C. P. Slichter, *Principles of magnetic resonance*, Vol. 1 (Springer Science & Business Media, 2013).
 - [2] L. M. K. Vandersypen and I. L. Chuang, *Rev. Mod. Phys.* **76**, 1037 (2005).
 - [3] C. L. Degen, F. Reinhard, and P. Cappellaro, *Rev. Mod. Phys.* **89**, 035002 (2017).
 - [4] A. L. Bloom, *Appl. Opt.* **1**, 61 (1962).
 - [5] W. Chalupczak and P. Josephs-Franks, *Phys. Rev. Lett.* **115**, 033004 (2015).
 - [6] P. Bevington, R. Gartman, and W. Chalupczak, *J. Appl. Phys.* **130**, 214501 (2021).
 - [7] H. G. Robinson and T. Myint, *Appl. Phys. Lett.* **5**, 116 (1964).
 - [8] A. Yoshimi, K. Asahi, K. Sakai, M. Tsuda, K. Yogo, H. Ogawa, T. Suzuki, and M. Nagakura, *Phys. Lett. A* **304**, 13 (2002).
 - [9] M. Jiang, H. Su, Z. Wu, X. Peng, and D. Budker, *Sci. Adv.* **7**, eabe0719 (2021).
 - [10] H. Su, M. Jiang, and X. Peng, *Sci. China Inf. Sci.* **65**, 200501 (2022).
 - [11] T. E. Chupp, R. J. Hoare, R. L. Walsworth, and B. Wu, *Phys. Rev. Lett.* **72**, 2363 (1994).
 - [12] R. E. Stoner, M. A. Rosenberry, J. T. Wright, T. E. Chupp, E. R. Oteiza, and R. L. Walsworth, *Phys. Rev. Lett.* **77**, 3971 (1996).
 - [13] D. Bear, T. E. Chupp, K. Cooper, S. DeDeo, M. Rosenberry, R. E. Stoner, and R. L. Walsworth, *Phys. Rev. A* **57**, 5006 (1998).
 - [14] T. Sato, Y. Ichikawa, S. Kojima, C. Funayama, S. Tanaka, T. Inoue, A. Uchiyama, A. Gladkov, A. Takamine, Y. Sakamoto, Y. Ohtomo, C. Hirao, M. Chikamori, E. Hikota, T. Suzuki, M. Tsuchiya, T. Furukawa, A. Yoshimi, C. P. Bidinosti, T. Ino, H. Ueno, Y. Matsuo, T. Fukuyama, N. Yoshinaga, Y. Sakemi, and K. Asahi, *Phys. Lett. A* **382**, 588 (2018).
 - [15] P. Bevington, R. Gartman, Y. V. Stadnik, and W. Chalupczak, *Phys. Rev. A* **102**, 032804 (2020).
 - [16] M. A. Rosenberry and T. E. Chupp, *Phys. Rev. Lett.* **86**, 22 (2001).
 - [17] T. Inoue, T. Furukawa, A. Yoshimi, T. Nanao, M. Chikamori, K. Suzuki, H. Hayashi, H. Miyatake, Y. Ichikawa, M. Tsuchiya, N. Hatakeyama, S. Kagami, M. Uchida, H. Ueno, Y. Matsuo, T. Fukuyama, and K. Asahi, *Eur. Phys. J. D* **70**, 129 (2016).
 - [18] D. Bear, R. E. Stoner, R. L. Walsworth, V. A. Kostelecký, and C. D. Lane, *Phys. Rev. Lett.* **85**, 5038 (2000).
 - [19] M. S. Safronova, D. Budker, D. DeMille, D. F. J. Kimball, A. Derevianko, and C. W. Clark, *Rev. Mod. Phys.* **90**, 025008 (2018).
 - [20] W. A. Terrano and M. V. Romalis, *Quantum Sci. Technol.* **7**, 014001 (2021).
 - [21] M. G. Richards, B. P. Cowan, M. F. Secca, and K. Machin, *J. Phys. B: At. Mol. Opt. Phys.* **21**, 665 (1988).
 - [22] G. D. Cates, S. R. Schaefer, and W. Happer, *Phys. Rev. A* **37**, 2877 (1988).
 - [23] D. D. McGregor, *Phys. Rev. A* **41**, 2631 (1990).
 - [24] M. V. Romalis and W. Happer, *Phys. Rev. A* **60**, 1385 (1999).
 - [25] See Supplementary Materials for more details.
 - [26] E. Hikota *et al.*, *EPJ Web Conf.* **66**, 05005 (2014).

Supplemental Materials: Feedback Assisted Spin Dynamics in an Inhomogeneous Bias Magnetic Field

I. DIMENSION REDUCTION

Given the initial condition $\mathbf{P}_1(t=0) = \mathbf{P}_2(t=0)$, we can prove that the equalities, $P_{1,z} = P_{2,z}$ and $P_{1,x}^2 + P_{1,y}^2 = P_{2,x}^2 + P_{2,y}^2$, hold for all time in the following way. Using Eqs. (1,2,3) in the main text, we find that the quantities $\Delta P_z \equiv P_{1,z} - P_{2,z}$ and $|P_{1,T}|^2 - |P_{2,T}|^2$ satisfy

$$\frac{d}{dt}\Delta P_z = -(G + 1/T_1)\Delta P_z - \alpha(|P_{1,T}|^2 - |P_{2,T}|^2)/2, \quad (\text{S1})$$

$$\frac{d}{dt}(|P_{1,T}|^2 - |P_{2,T}|^2) = (\alpha\bar{P}_z - 2/T_2)(|P_{1,T}|^2 - |P_{2,T}|^2) + 2\alpha|\bar{P}_T|^2\Delta P_z. \quad (\text{S2})$$

Since $\Delta P_z(t=0) = 0$ and $|P_{1,T}(t=0)|^2 - |P_{2,T}(t=0)|^2 = 0$, from Eqs. (S1) and (S2), one can prove by induction that any order derivatives of $\Delta P_z(t)$ and $|P_{1,T}(t)|^2 - |P_{2,T}(t)|^2$ are zero at $t=0$. Therefore the two equalities $\Delta P_z(t) = 0$ and $|P_{1,T}(t)|^2 - |P_{2,T}(t)|^2 = 0$ must hold all the time.

The condition $|P_{1,T}(t)|^2 - |P_{2,T}(t)|^2 = 0$ means that \bar{P}_T must be orthogonal to $\Delta P_T \equiv P_{1,T} - P_{2,T}$ in the complex plane. So parameterizing $\bar{P}_T = Ae^{i\theta}/2$ and $\Delta P_T = Be^{i(\theta+\pi/2)}$ with the amplitudes A and B and the phase angle θ being real and combining the Bloch equations in the main text with the two constraints, we have

$$\frac{dA}{dt} = \alpha\bar{P}_z A + \epsilon B/2 - A/T_2, \quad (\text{S3})$$

$$\frac{dB}{dt} = -\epsilon A/2 - B/T_2, \quad (\text{S4})$$

$$\frac{d\bar{P}_z}{dt} = -\alpha A^2/4 - \bar{P}_z/T_1 + G(P_0 - \bar{P}_z), \quad (\text{S5})$$

$$\frac{d\theta}{dt} = -\omega_c. \quad (\text{S6})$$

The phase angle can be readily solved as $\theta(t) = -\omega_c t + \phi$. The remaining dimensions of the dynamic system are reduced to be three.

Even for initial condition $\mathbf{P}_1(t=0) \neq \mathbf{P}_2(t=0)$, by numerical calculation, we find the two equalities, $P_{1,z} = P_{2,z}$ and $|P_{1,T}|^2 = |P_{2,T}|^2$ with $P_{j,T} \equiv P_{j,x} + iP_{j,y}$, are maintained by the stable dynamics in a wide parameter range [see Fig. 1 in the main text]; the following Fig. S1 shows typical behaviors of such dynamics.

II. LINEAR STABILITY ANALYSIS

The stable regions of the no signal fixed point and limit cycles can be derived analytically via the linear stability analysis.

A. Binary Larmor Frequencies

In the case of binary Larmor frequencies, since both the no signal fixed point and limit cycles maintain $P_{1,z} = P_{2,z}$ and $P_{1,x}^2 + P_{1,y}^2 = P_{2,x}^2 + P_{2,y}^2$, we apply the dimension reduction and turn to study Eqs. (S3) to (S5). In terms of $\{A, B, \bar{P}_z\}$, the steady state equations are given by

$$0 = \alpha\bar{P}_z A + \epsilon B/2 - A/T_2, \quad (\text{S7})$$

$$0 = -\epsilon A/2 - B/T_2, \quad (\text{S8})$$

$$0 = -\alpha A^2/4 - \bar{P}_z/T_1 + G(P_0 - \bar{P}_z). \quad (\text{S9})$$

By solving the above equations, we obtain two solutions. One is the no signal fixed point $A_{\text{NS}} = B_{\text{NS}} = 0$ and $\bar{P}_{z,\text{NS}} = P_0(1 + 1/GT_1)$. Another one is a pair of twin fixed points $A_{\text{LC},\pm} = \pm 2\{GP_0[\alpha - \alpha_c f(\epsilon)]\}^{1/2}/\alpha$, $B_{\text{LC},\pm} = -T_2\epsilon A_{\text{LC},\pm}/2$ and $\bar{P}_{z,\text{LC}} = f(\epsilon)/\alpha T_2$ with $f(\epsilon) \equiv [1 + (\epsilon T_2/2)^2]$, which corresponds to the limit cycles in terms of \mathbf{P}_j as described in the main text.

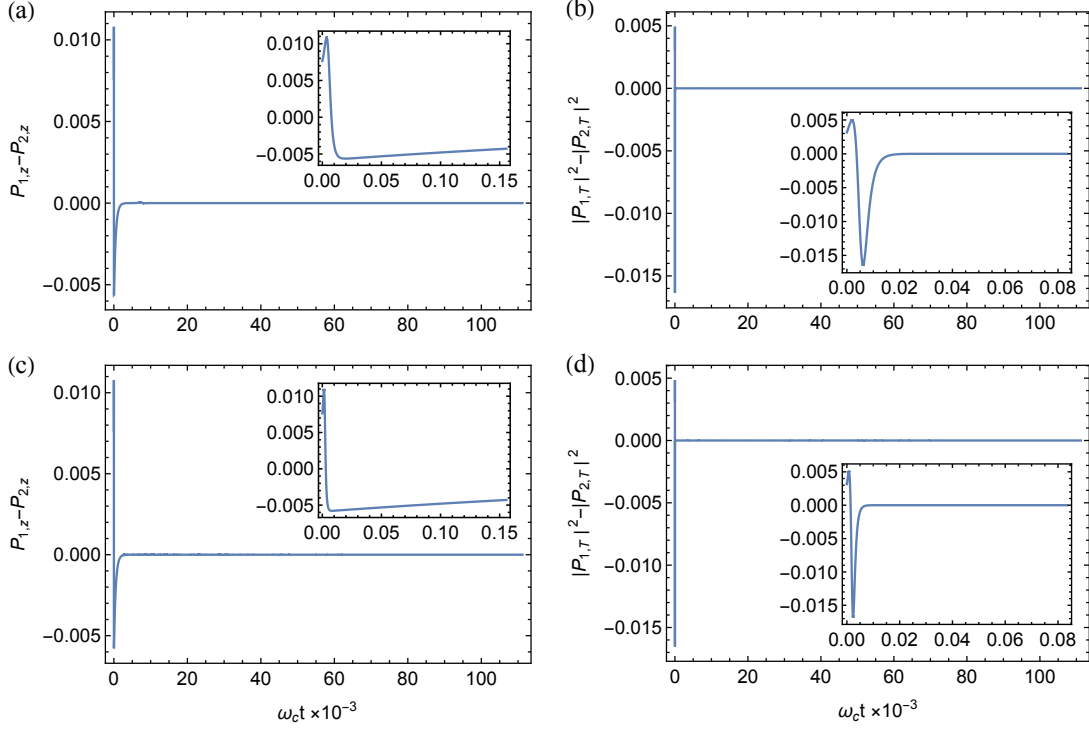


FIG. S1: Time evolution of quantities $P_{1,z} - P_{2,z}$ and $|P_{1,T}|^2 - |P_{2,T}|^2$. (a)~(b) are for $\alpha/\alpha_c = 3$ and $\epsilon T_2 = 3$ where the stable dynamics is quasi-periodic orbits. (c)~(d) are for $\alpha/\alpha_c = 7.8$ and $\epsilon T_2 = 2$ where the stable dynamics is chaos. The initial conditions are chosen such that $\mathbf{P}_1(t=0) = (\sin(\pi/15), 0, \cos(\pi/15))$, $\mathbf{P}_2(t=0) = (\sin(\pi/16), 0, \cos(\pi/16))$.

First, let us look at the stability of the no signal fixed point. We expand as $A = A_{\text{NS}} + \delta A$, $B = B_{\text{NS}} + \delta B$ and $\bar{P}_z = \bar{P}_{z,\text{NS}} + \delta \bar{P}_z$, and solve Eqs. (S3) to (S5) to the first order of the variations δA , δB and $\delta \bar{P}_z$; the resulting linearized equations read

$$\frac{d\delta A}{dt} = (\alpha \bar{P}_{z,\text{NS}} - 1/T_2) \delta A + \epsilon \delta B/2, \quad (\text{S10})$$

$$\frac{d\delta B}{dt} = -\epsilon \delta A/2 - \delta B/T_2, \quad (\text{S11})$$

$$\frac{d\delta \bar{P}_z}{dt} = -(1/T_1 + G) \delta \bar{P}_z. \quad (\text{S12})$$

$\delta \bar{P}_z$ would always decay exponentially, and the growth rates regarding δA and δB are given by

$$\lambda_{\text{NS},\pm} = \frac{1}{2T_2} \left\{ \alpha/\alpha_c - 2 \pm [(\alpha/\alpha_c)^2 - (\epsilon T_2)^2]^{1/2} \right\}. \quad (\text{S13})$$

We analyze the condition when $\text{Re}(\lambda_{\text{NS},\pm})$ turn to be positive.

i) $\alpha/\alpha_c > \epsilon T_2$. In this case, $\text{Re}(\lambda_{\text{NS},\pm}) > 0$ requires

$$\alpha/\alpha_c - 2 \pm [(\alpha/\alpha_c)^2 - (\epsilon T_2)^2]^{1/2} > 0 \quad (\text{S14})$$

For $\alpha/\alpha_c > 2$, $\text{Re}(\lambda_{\text{NS},+})$ is always positive. On the other hand $\text{Re}(\lambda_{\text{NS},-}) > 0$ requires

$$2 < \alpha/\alpha_c < 1 + \left(\frac{\epsilon T_2}{2} \right)^2, \quad (\text{S15})$$

which is possible if $\epsilon T_2 > 2$.

For $\alpha/\alpha_c < 2$, $\text{Re}(\lambda_{\text{NS},-})$ is always negative. And $\text{Re}(\lambda_{\text{NS},+}) > 0$ requires

$$1 + \left(\frac{\epsilon T_2}{2} \right)^2 < \alpha/\alpha_c < 2, \quad (\text{S16})$$

which is possible if $\epsilon T_2 < 2$.

ii) $\alpha/\alpha_c < \epsilon T_2$. In this case, $\text{Re}(\lambda_{\text{NS},\pm}) > 0$ requires

$$2 < \alpha/\alpha_c < \epsilon T_2. \quad (\text{S17})$$

which is possible if $\epsilon T_2 > 2$.

In summary, the no signal fixed point is stable when $\alpha/\alpha_c < 1 + (\epsilon T_2/2)^2$ for $\epsilon T_2 < 2$, and $\alpha/\alpha_c < 2$ for $\epsilon T_2 > 2$. For $\epsilon T_2 < 2$, when $\alpha/\alpha_c > 1 + (\epsilon T_2/2)^2$, the fixed point becomes unstable in one direction while for $\epsilon T_2 > 2$, when $\alpha/\alpha_c > 2$, the fixed point becomes unstable in two directions.

The stability of the limit cycles can be analyzed in the same way. Similar linearization around $A_{\text{LC},\pm}$, $B_{\text{LC},\pm}$ and $\bar{P}_{z,\text{LC}}$ gives

$$\frac{d\delta A}{dt} = (\alpha \bar{P}_{z,\text{LC}} - 1/T_2)\delta A + \epsilon \delta B/2 + \alpha A_{\text{LC},\pm} \delta \bar{P}_z, \quad (\text{S18})$$

$$\frac{d\delta B}{dt} = -\epsilon \delta A/2 - \delta B/T_2, \quad (\text{S19})$$

$$\frac{d\delta \bar{P}_z}{dt} = -\alpha A_{\text{LC},\pm} \delta A/2 - (1/T_1 + G)\delta \bar{P}_z, \quad (\text{S20})$$

which give the characteristic equation for the growth rate β

$$\beta^3 + a\beta^2 + b\beta + c = 0, \quad (\text{S21})$$

with

$$a = G + 1/T_1 + [2 - f(\epsilon)]/T_2, \quad (\text{S22})$$

$$b = GP_0 [2\alpha - 3f(\epsilon)\alpha_c + 2\alpha_c], \quad (\text{S23})$$

$$c = \alpha^2 A_{\text{LC},\pm}^2 / (2T_2), \quad (\text{S24})$$

Here the reality of a, b, c and $c > 0$ guarantee that one root of the characteristic equation must be real and negative. It turns out that the limit cycles become unstable when a pair of complex conjugate roots cross the imaginary axis, which corresponds to a Hopf bifurcation. So we insert $\beta = i\Omega$ into the characteristic Eq. (S21) and obtain $\Omega^2 = b$ and $\Omega^2 = c/a$. The reality of Ω demands $b > 0$ and $c/a > 0$, meanwhile the limit cycles becomes unstable when $c = ab$, namely

$$\alpha/\alpha_c = g(y) \equiv 3y/2 + (1-d)/[2(y-d)], \quad (\text{S25})$$

where $y \equiv (\epsilon T_2/2)^2$ and $d \equiv T_2(G + 1/T_1)$. Physically the transition curve $g(y)$ must lie in the region that the limit cycle solution exists, which demands $g(y) > f(y)$. To assure that condition, we need to look at

$$\begin{aligned} g(y) - f(y) &= y/2 + (1-d)/[2(y-d)] - 1 \\ &= (y-1)(y-1-d)/[2(y-d)]. \end{aligned} \quad (\text{S26})$$

We then consider different cases to determine the transition curves.

i) $y < 1$. In this case, $b > 0$ and $c/a > 0$ are surely satisfied. We can see from Eq. (S26) that $g(y) < f(y)$ for $d > 1$. For $d < 1$, $g(y) > f(y)$ is satisfied in the region $d < y < 1$.

ii) $y > 1$. In this case, $b > 0$ and $c/a > 0$ demand

$$\alpha/\alpha_c > (1+3y)/2, \quad (\text{S27})$$

$$1 < y < 1+d. \quad (\text{S28})$$

Since $1 < y < 1+d$, it can be seen that $g(y) > f(y)$ is satisfied in the region $1 < y < d$ and $d > 1$ is implied here. Meanwhile $g(y)$ must lie in the region $\alpha/\alpha_c > (1+3y)/2$, which demands $g(y) - (1+3y)/2 = (1-y)/[2(y-d)] > 0$. This is also satisfied in the region $1 < y < d$.

In summary, the limit cycles become unstable at the transition curve $\alpha/\alpha_c = g(y)$ for $\text{Min}(1, d) < y < \text{Max}(1, d)$.

B. Continuum Limit

In the continuum limit, the Bloch equations becomes

$$\frac{dP_x(\omega)}{dt} = \omega P_y(\omega) + \alpha \bar{P}_x P_z(\omega) - \frac{P_x(\omega)}{T_2}, \quad (\text{S29})$$

$$\frac{dP_y(\omega)}{dt} = -\omega P_x(\omega) + \alpha \bar{P}_y P_z(\omega) - \frac{P_y(\omega)}{T_2}, \quad (\text{S30})$$

$$\frac{dP_z(\omega)}{dt} = -\alpha [\bar{P}_x P_x(\omega) + \bar{P}_y P_y(\omega)] - \frac{P_z(\omega)}{T_1} + G[P_0 - P_z(\omega)], \quad (\text{S31})$$

By transforming to the rotating frame $\tilde{P}_T(\omega) = e^{i\omega_s t} P_T(\omega)$ and $\tilde{\bar{P}}_T = e^{i\omega_s t} \bar{P}_T$ with $P_T(\omega) \equiv P_x(\omega) + iP_y(\omega)$, we derive

$$\frac{d\tilde{P}_T(\omega)}{dt} = i(\omega_s - \omega) \tilde{P}_T(\omega) + \alpha \tilde{\bar{P}}_T(\omega) P_z(\omega) - \frac{\tilde{P}_T(\omega)}{T_2}, \quad (\text{S32})$$

$$\frac{d\tilde{P}_T^*(\omega)}{dt} = -i(\omega_s - \omega) \tilde{P}_T^*(\omega) + \alpha \tilde{\bar{P}}_T^*(\omega) P_z(\omega) - \frac{\tilde{P}_T^*(\omega)}{T_2}, \quad (\text{S33})$$

$$\frac{dP_z(\omega)}{dt} = -\frac{\alpha}{2} [\tilde{P}_T \tilde{P}_T^*(\omega) + \tilde{\bar{P}}_T^* \tilde{P}_T(\omega)] - \frac{P_z(\omega)}{T_1} + G[P_0 - P_z(\omega)]. \quad (\text{S34})$$

By equating the left sides of Eqs. (S32) to (S34) to zero, we can obtain either the no signal fixed point, which corresponds to $\tilde{P}_T = 0$, or the limit cycle solution, which corresponds to $\tilde{P}_T \neq 0$.

The matrix \mathcal{M} in the main text can be obtained by assuming $\delta\tilde{P}_T(\omega) = e^{\beta t} F(\omega)$ and $\delta P_z(\omega) = e^{\beta t} G(\omega)$ around the solutions above with $F(\omega)$ a complex function and $G(\omega)$ a real one and β the growth rate, which satisfies the linearized Bloch equations

$$\mathcal{M} \begin{bmatrix} \delta P_z(\omega) \\ \delta \tilde{P}_T(\omega) \\ \delta \tilde{P}_T^*(\omega) \end{bmatrix} = \begin{bmatrix} -\alpha[\delta \tilde{P}_T^* \tilde{P}_T(\omega) + \delta \tilde{\bar{P}}_T^* \tilde{P}_T^*(\omega)]/2 \\ \alpha P_z(\omega) \delta \tilde{P}_T \\ \alpha P_z(\omega) \delta \tilde{P}_T^* \end{bmatrix}. \quad (\text{S35})$$

Via Eq. (S35), we solve $\delta\tilde{P}_T(\omega)$ and $\delta\tilde{P}_T^*(\omega)$ in terms of $\delta\tilde{P}_T$ and $\delta\tilde{P}_T^*$. By using $\delta\tilde{P}_T = \int_{-\infty}^{\infty} d\omega \rho(\omega) \delta\tilde{P}_T(\omega)$, we find the characteristic equation determining the growth rate β as described in the main text.

III. PHASE PORTRAITS

We have seen in the main text that for the case of binary Larmor frequencies, the dimension reduction simplifies the analysis and visualization of the trajectories of the quasi-periodic orbits and chaos when it is applicable. Especially the quasi-periodic orbits unify into a limit cycle solution in terms of $\{A, B, \bar{P}_z\}$. The period τ of this emergent limit cycle solution in general depends on α/α_c and ϵT_2 . Figure S2 plots $1/\tau$ versus ϵ for $\alpha/\alpha_c = 2.46$. In the limit $\epsilon T_2 \rightarrow \infty$, $1/\tau$ is found to be proportional to ϵT_2 as expected from Eqs. (S3) to (S5). The period τ seems to diverge when ϵT_2 approaches 1.787, the stable boundary for the quasi-periodic orbits. The divergence indicates a homoclinic bifurcation. Even when the dimension reduction is not applicable, the phase portraits of the quasi-periodic orbits and chaos retain their characteristics as shown in Fig. S3. The phase portraits of the stable dynamics in the continuum limit are similar, which are plotted for the triangle distribution in Figure S4.

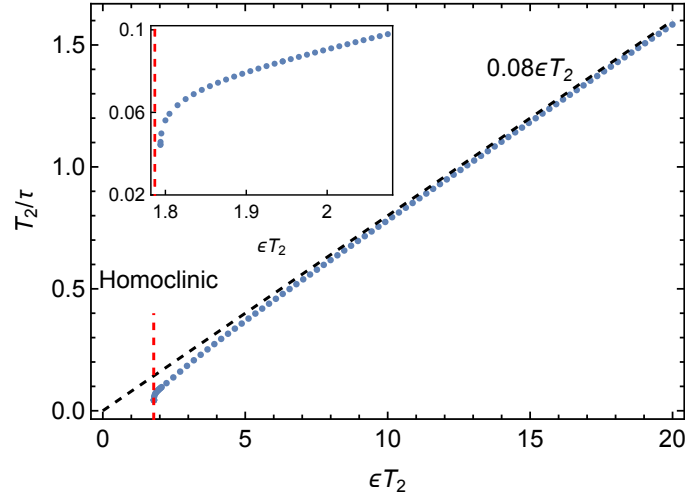


FIG. S2: The period of the unified limit cycle in terms of A, B, P_z for $\alpha/\alpha_c = 2.46$. A black dashed line $0.08\epsilon T_2$ is plotted for reference. Red dashed line indicates the position of homoclinic bifurcation. Subfigure shows the details near homoclinic bifurcation.

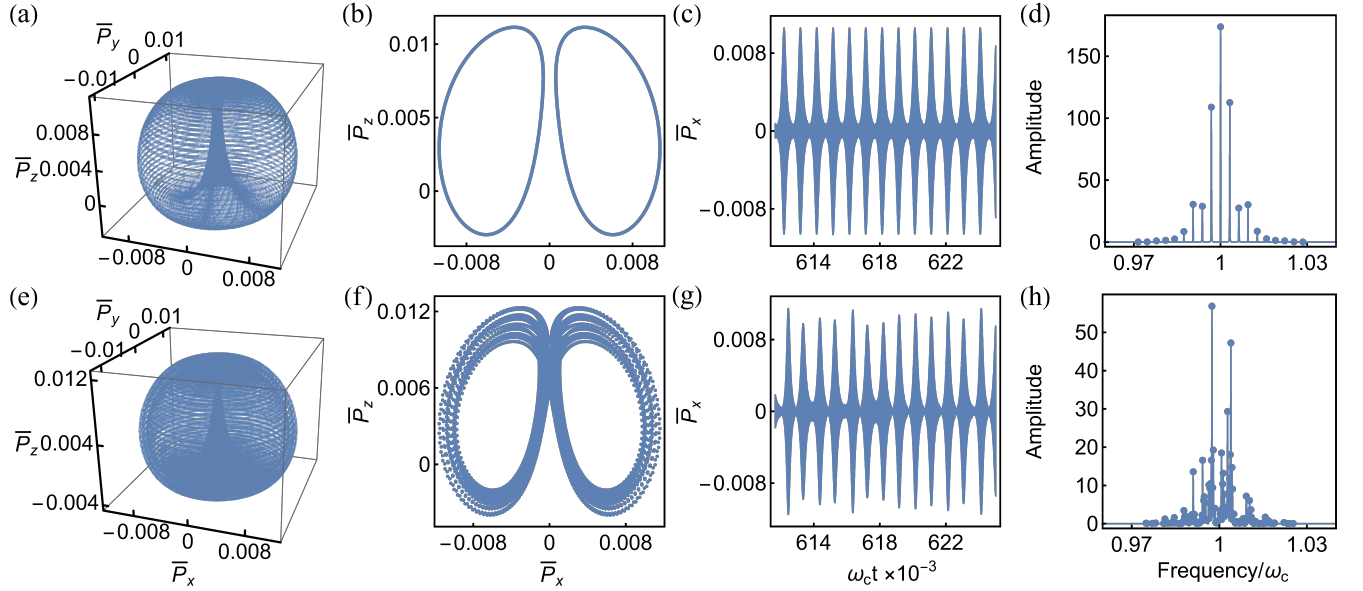


FIG. S3: Stable dynamic behaviors of quasi-period orbits (top row) and chaos (bottom row) for the case of binary Larmor frequencies with $\Delta P_z(t) = 0$ and $|P_{1,T}(t)|^2 - |P_{2,T}(t)|^2 = 0$ violated. The first column of the graphs plot the trajectories of the average spin $\bar{\mathbf{P}}(t)$, and the second are the corresponding trajectories intersecting the plain of $\bar{P}_y = 0$. The third column show the time series of $\bar{P}_x(t)$ and the forth are the Fourier transform amplitudes of $\bar{P}_x(t)$ in arbitrary units. Parameters here are $\alpha/\alpha_c = 7.38$, $\epsilon T_2 = 1.75$ for (a)~(d), and $\alpha/\alpha_c = 7.38$, $\epsilon T_2 = 1.87$ for (e)~(h).

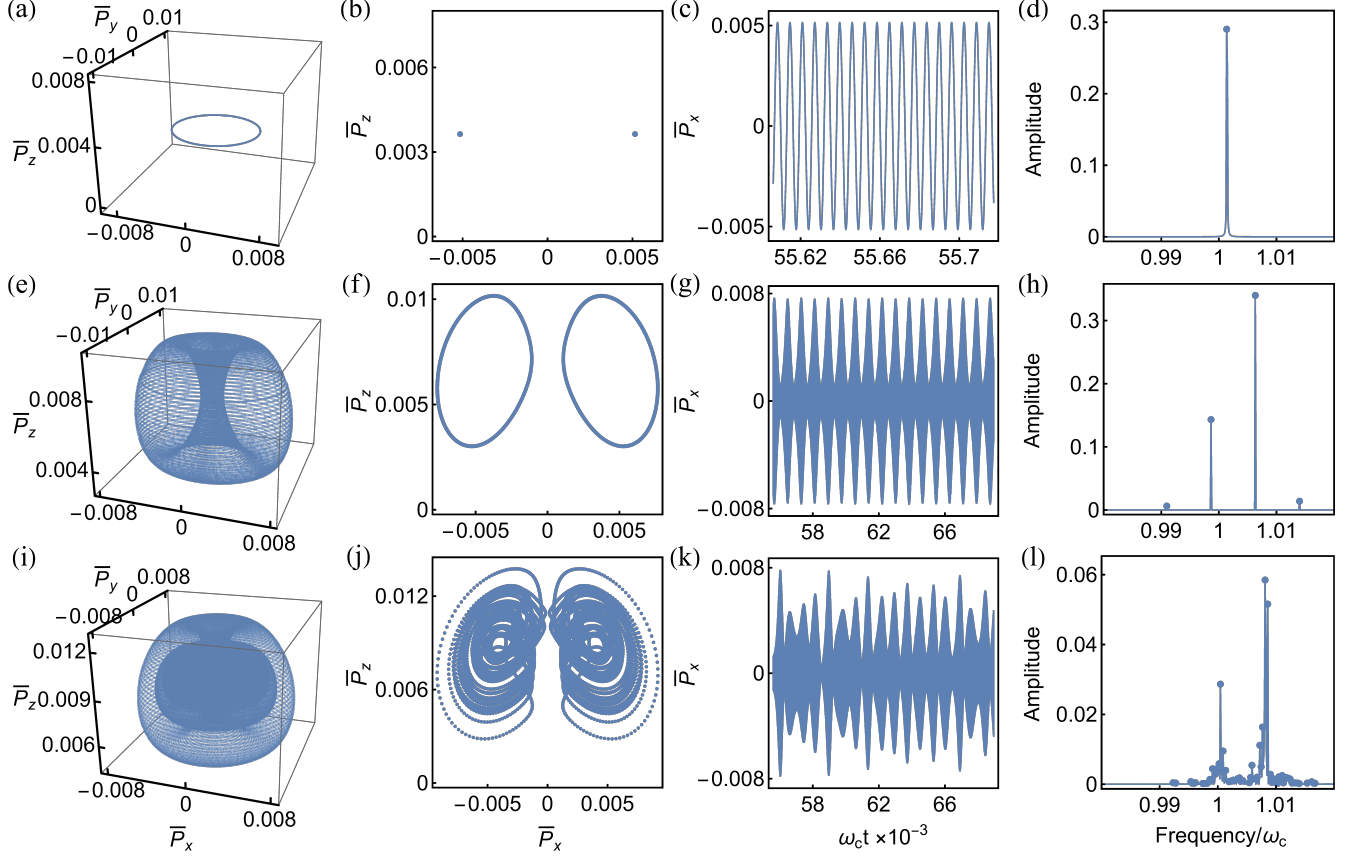


FIG. S4: Stable dynamic behaviors of the limit cycles (top row), quasi-period orbits (middle row) and chaos (bottom row) for the triangle distribution $\rho_T(\omega)$ in the continuum limit. The first column of the graphs plot the trajectories of the average spin $\bar{\mathbf{P}}(t)$, and the second are the corresponding trajectories intersecting the plane of $\bar{P}_y = 0$. The third column show the time series of $\bar{P}_x(t)$ and the forth are the Fourier transform amplitudes of $\bar{P}_x(t)$ in arbitrary units. Parameters here are $\alpha/\alpha_c = 7$, $\epsilon T_2 = 3$ for (a)~(d), $\alpha/\alpha_c = 7$, $\epsilon T_2 = 8$ for (e)~(h), and $\alpha/\alpha_c = 7$, $\epsilon T_2 = 11$ for (i)~(l).